


Selectively monitoring the operando temperature of active metal nanoparticles during catalytic reactions by X-ray absorption nanothermometry

Received: 20 March 2024

Accepted: 2 January 2025

Published online: 04 February 2025

 Check for updates

Matthias Filez^{1,2}✉, Valentijn De Coster³, Hilde Poelman³, Valerie Briois⁴, Anthony Beauvois⁴, Jolien Dendooven¹, Maarten B. J. Roeffaers², Vladimir Galvita³ & Christophe Detavernier¹✉

Heat involved in catalytic reactions can influence the local temperature and performance of the active site, potentially causing catalyst degradation and runaway scenarios. Yet, broadly applicable thermometry methods to selectively probe the temperature of the catalytically active phase—where reactions take place—are generally lacking. Here we explore extended X-ray absorption fine-structure thermometry to monitor the operando temperature of active Ni nanoparticles, fully deconvoluted from their metal-oxide support. During dry reforming of methane, the reaction's endothermicity causes Ni nanoparticles to become local heat sinks with their temperature deviating 90 °C from the reactor temperature. By thermometry at the single nanoparticle level, we chart the energy balance of nanoparticles and relate their temperature to reaction kinetics. Covering the full temperature range relevant to catalysis, this broadly applicable method enables temperature monitoring of individual catalyst components separately. Applying extended X-ray absorption fine-structure thermometry to existing datasets worldwide can generate enhanced understanding on reaction-induced temperature phenomena in heterogeneous catalysis.

Temperature is a key parameter influencing the kinetics and thermodynamics of chemical reactions and, hence, governs the performance of a catalyst^{1–4}. However, in the past century, the main research focus has been on charting the structure of catalysts, preferably under in situ or operando conditions, to construct structure–performance relations^{5–20}. By contrast, monitoring the catalyst temperature has generally been disregarded due to characterization challenges and is assumed constant to the temperature of the reactor unit as a whole. Nevertheless, chemical reactions commonly exhibit exothermic or endothermic

characteristics, resulting in the release or uptake of heat at the active surface of the catalyst. This results in local temperature changes of the active phase²¹, which may deviate from the reactor temperature as a whole, and alters the local performance accordingly. Consequently, there is a stringent need to lift this often-forgotten temperature dimension in catalyst investigations to revisit how catalysts work.

Only a handful of characterization tools have been explored to directly probe the catalyst temperature, most recently via light^{22,23} rather than thermocouples. For example, infrared (IR) thermometry^{24–26}

¹Conformal Coating of Nanomaterials, Department of Solid State Sciences, Ghent University, Ghent, Belgium. ²Centre for Membrane Separations, Adsorption, Catalysis and Spectroscopy for Sustainable Solutions, KU Leuven, Leuven, Belgium. ³Laboratory for Chemical Technology, Ghent University, Ghent, Belgium. ⁴SOLEIL Synchrotron, L'Orme des Merisiers, Saint Aubin, France. ✉e-mail: matthias.filez@ugent.be; christophe.detavernier@ugent.be

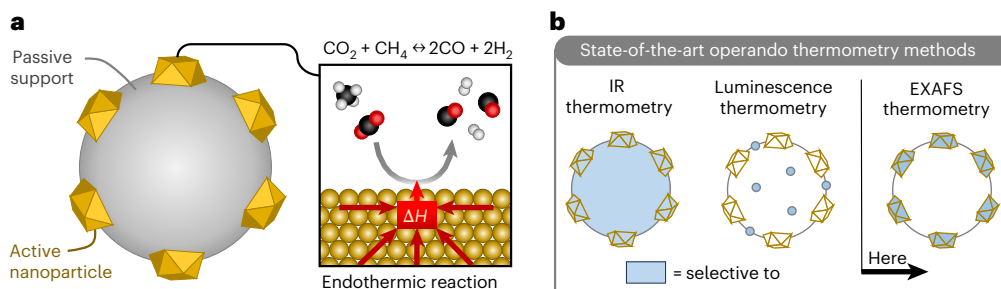


Fig. 1 | Schematic illustration of the concept of this study. **a**, A nanocatalyst consisting of active nanoparticles (gold) anchored on a passive support (grey). The nanoparticles facilitate reaction at their surface (black frame), for example, endothermic DRM ($\text{CO}_2 + \text{CH}_4 = 2\text{CO} + 2\text{H}_2$), leading to heat uptake from the nanoparticle proportional to the enthalpy of reaction (ΔH). **b**, State-of-the-art operando thermometry methods to probe reaction-induced temperature

changes in heterogeneous catalysts. The blue shaded areas illustrate the catalyst components for which the methods are temperature sensitive: support and active nanoparticles for IR thermometry, luminescent nanoparticles for luminescence thermometry and active nanoparticles only for EXAFS thermometry.

has been applied to chart the catalyst temperature across a catalytic bed, showing that the catalyst temperature can deviate hundreds of degrees from the set temperature of the reactor. Recently, Weckhuysen and collaborators^{27–31} pioneered luminescence thermometry by incorporating luminescent sensors in the catalyst architecture, which function as internal temperature read out reporters. It was demonstrated that temperature fluctuations occur in the catalyst when changing the gas feed composition^{28,31}. This further underpins the importance of operando monitoring the local catalyst temperature and the need for advanced thermometry tools.

While already an impressive advancement, current state-of-the-art thermometry methods lack the ability to selectively monitor the temperature of the catalytically active phase, where the most extreme temperature perturbations are expected. In the case of many supported nanoparticle catalysts, the nanoparticles constitute the active phase responsible for catalytic reaction, while the support can remain a passive spectator (Fig. 1a). Importantly, nanoparticles typically represent only a small fraction of the total catalyst mass³² (1–5%), whereas IR and luminescence thermometry monitor the temperature of the catalyst as a whole. Consequently, these methods predominantly probe the temperature of the passive support while staying virtually blind to the active nanoparticles that can form local hotspots or heat sinks during catalytic reaction (Fig. 1b).

Selectively probing the temperature of individual catalyst phases has been proven possible by monitoring their temperature-dependent magnetic properties. For example, ²⁷Al nuclear magnetic resonance³³ has been applied to monitor the support temperature of Pd/ γ -Al₂O₃ catalysts, while the Ni crystallite temperature of Ni/SiO₂ could be extracted via their superparamagnetic³⁴ properties. However, these methods are applicable to only a very small subset of relevant catalytic systems and, hence, not generally exploitable, while also challenging to implement. A technique that is widely applicable and non-invasive and displays marked selectivity to the phase of interest is extended X-ray absorption fine-structure (EXAFS) thermometry³⁵. Although still largely unexplored, this method has demonstrated abilities to probe the temperature of laser, microwave or inductively heated nanoparticles, for example, in nanomedicine for cancer treatment^{36–39}. Thus far, EXAFS thermometry has not been applied in thermal catalysis to probe the operando temperature changes of nanoparticles induced by reaction heat effects.

Here, we analyse the possible application of operando EXAFS thermometry to monitor the dynamic temperature evolution of active Ni nanoparticles during catalytic CO₂ conversion reactions, namely the dry reforming of methane (DRM) and reverse water gas shift (RWGS) reactions. During endothermic reaction, heat uptake from the Ni nanoparticles causes a decrease in nanoparticle temperature and the

associated thermal disorder in the nanoparticle lattice. The atomic disorder causes damping of the EXAFS signal, which is here instrumentalized to selectively extract the temperature of active Ni nanoparticles, fully deconvoluted from the passive support. We further demonstrate that this method is applicable in the full temperature range relevant to catalysis (<800 °C) and showcase that detailed temperature profiles can be extracted even at temperatures as high as 750 °C—where other thermometry methods are more prone to failure. During DRM, we observe a transient temperature decay of 90 °C on a 2 h timescale, significantly deviating from the set reactor temperature. In addition, for the exothermic CO₂ methanation reaction, a mild temperature rise is observed in active Ni nanoparticles. By accurate temperature bookkeeping at the nanoparticle level, we can chart the energy balance of nanoparticles and relate their temperature changes to catalytic reaction kinetics.

Results

EXAFS–temperature relation

The temperature of a nanoparticle results from its thermal energy, which introduces vibrations and structural disorder at the atomic scale. When evolving from low to high temperatures, the atomic lattice becomes more disordered (Fig. 2a). This results in a more irregular coordination sphere (Fig. 2a, gold atoms) around the central atom (Fig. 2a, purple atom), yielding a bond length distribution around the central atom with decreased height and larger width (Fig. 2b). EXAFS heavily depends on this bond length distribution and, hence, on the lattice temperature. By inverting this reasoning, the temperature dependency of EXAFS can be instrumentalized to extract the temperature of nanoparticles during catalysis.

To achieve this, first, an EXAFS–temperature relation needs to be established. Therefore, in situ quick X-ray absorption spectroscopy (QXAS) is acquired on a prereduced bulk Ni powder during H₂ temperature-programmed reduction (TPR) at the Ni K-edge while recording temperature (ROCK beamline, SOLEIL synchrotron⁴⁰; Methods). The Ni temperature is assumed equal to the thermocouple temperature (Supplementary Note 1). The H₂–He flow during TPR assures that prereduced metallic Ni remains unmodified while acquiring EXAFS at various temperatures.

During TPR, the k^2 -weighted EXAFS signals $k^2\chi(k)$ recorded from 60 °C (Fig. 2d, blue) to 150 °C (Fig. 2d, red) show a gradual damping of the EXAFS oscillations with increasing temperature, especially at high k values. This is caused by the Debye–Waller disorder factor σ^2 , which dampens the EXAFS oscillations by a factor of $e^{-k^2\sigma^2}$ (ref. 41). The Debye–Waller factor scales to the width of the bond length distribution of the X-ray absorber–scatterer pairs (Fig. 2b). Hence, when the temperature of a material rises, the level of structural disorder goes up,

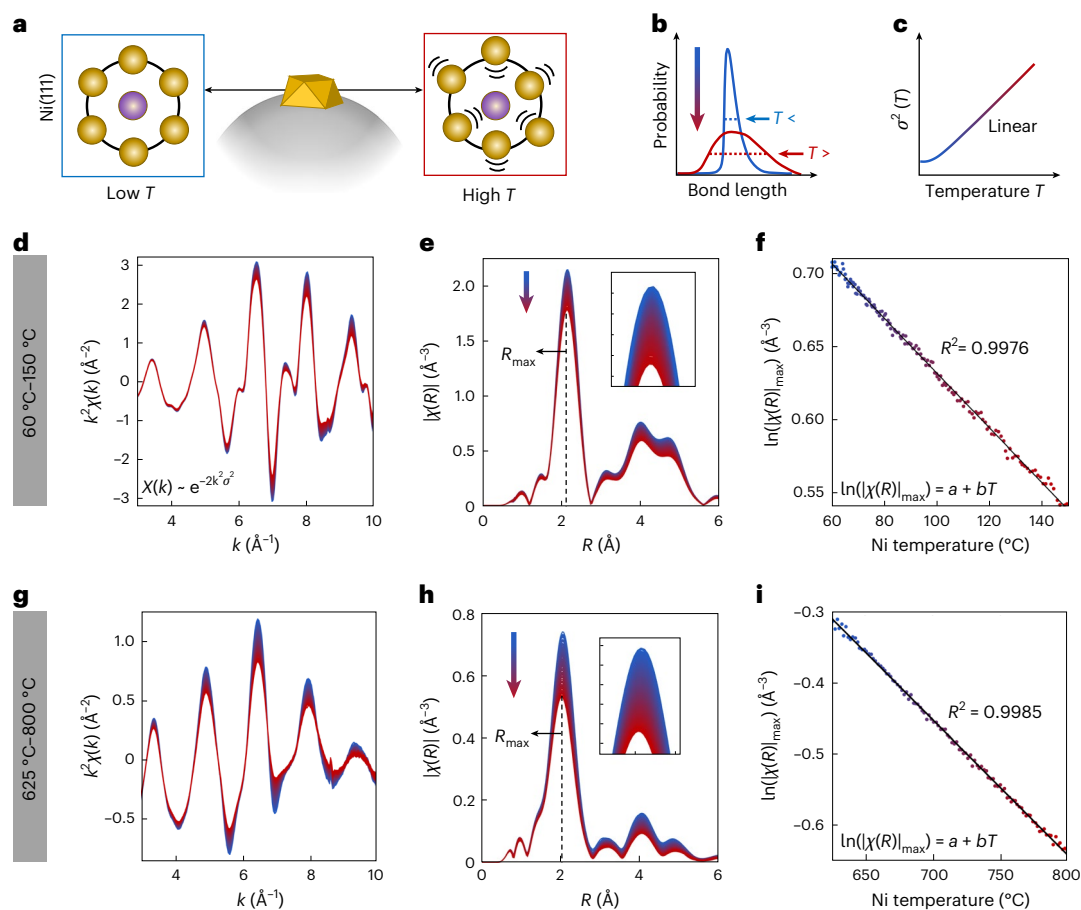


Fig. 2 | Establishing a relation between EXAFS and temperature. **a**, A schematic representation of the atomic structure in the core of a Ni nanoparticle at low temperature (blue frame) and high temperature (red frame), here showcased for a Ni(111) plane. The black circle indicates the average position of the Ni atoms in the first coordination shell (gold) around the central Ni atom (purple), the latter being the X-ray absorber during EXAFS. **b**, The radial distribution function at low (blue) and high (red) temperature around the central atom, plotted as a probability versus the radial distance from the central atom. The width of the distribution is indicated by the dashed line. **c**, The relationship between the Debye–Waller disorder factor σ^2 and the material temperature, showing a

quasi-linear dependency at higher temperatures. **d–i**, EXAFS–temperature calibration workflow in the low-temperature range (60–150 °C) (**d–f**) and high-temperature range (625–800 °C) (**g–i**), with k^2 -weighted EXAFS signals ($k^2\chi(k)$) measured at the Ni K-edge during H₂ TPR (**d** and **g**). The magnitude of the FT k^2 -weighted EXAFS signal ($|\text{FT}[k^2\chi(k)]| = |\chi(R)|$) (**e** and **h**) and the resulting linear relationship between $\ln(|\chi(R)|_{\text{max}})$ and the Ni temperature (**f** and **i**) are shown. In **d–i**, the colour code ranges from blue to red, corresponding to the lowest and highest temperature probed within the range. For example, blue is 60 °C (**d–f**) and 625 °C (**g–i**), and red is 150 °C (**d–f**) and 800 °C (**g–i**). The black lines (**f** and **i**) are linear fits through the data.

leading to a broader bond length distribution and an increased Debye–Waller factor, thus damping the EXAFS signal. More quantitatively, at higher temperatures, the Debye and Einstein models describe that $\sigma^2(T)$ follows a quasi-linear relation with the temperature T (Fig. 2c)⁴².

Damping of the $k^2\chi(k)$ EXAFS signal translates in a global decrease of the R -space EXAFS signal, being the magnitude of the Fourier-transformed (FT) EXAFS signal ($|\text{FT}[k^2\chi(k)]| = |\chi(R)|$; Fig. 2e). The FT EXAFS signal relates to the radial distribution function around the X-ray absorber, in this case Ni, plotted as a function of the interatomic distance R .

The EXAFS–temperature correlation is now extracted by plotting $\ln(|\chi(R)|_{\text{max}})$ versus the Ni temperature (Fig. 2f), where $|\chi(R)|_{\text{max}}$ is the maximal magnitude of the first Ni coordination shell in the FT EXAFS signal ($R_{\text{max}} \approx 2 \text{ \AA}$; Fig. 2e). $\ln(|\chi(R)|_{\text{max}})$ is a negative linear function of the Ni temperature, with low scatter ($R^2 = 0.9976$).

To demonstrate the generality of the approach, the same methodology is adopted in a high-temperature range relevant to catalysis, that is 625–800 °C (Fig. 2g–i). The linear relationship between $\ln(|\chi(R)|_{\text{max}})$ and the Ni temperature again demonstrates excellent agreement ($R^2 = 0.9985$). This underscores that the Ni temperature can be accurately extracted from the EXAFS–temperature relation over a

relatively wide temperature range (60–800 °C; Supplementary Fig. 1), relevant to thermal catalytic processes. The 95% confidence interval for the temperature is calculated in the low- and high-temperature range and respectively corresponds to 2.7 °C and 4.0 °C (Supplementary Fig. 2). Notably, this confidence interval could vary for catalysts with different composition (Supplementary Note 2).

EXAFS thermometry during CO₂ conversion to extract kinetics

By instrumentalizing the EXAFS–temperature relation (Fig. 2f,i), thermometry can now be applied to monitor the temperature of active nanoparticles during catalytic reaction. Therefore, a quartz capillary tube containing a catalyst bed with MgAl₂O₄-supported Ni nanoparticles (6.2 ± 2.2 nm; Supplementary Fig. 3) is positioned in an oven for homogeneous heat distribution (Fig. 3a). A thermocouple used for temperature control of the oven is positioned close to the end of the catalyst bed, within the quartz wool plug confining the bed. Operando QXAS is performed, yielding Ni K-edge spectra with 5 s time resolution. Two catalytic CO₂ conversion processes are run at a setpoint temperature of 750 °C, each time using an identical Ni/MgAl₂O₄ catalyst (Fig. 3b and Methods): DRM (CO₂ + CH₄ = 2CO + 2H₂), where the CO₂:CH₄ ratio is cycled between 2:1 and 1:1 in a period of

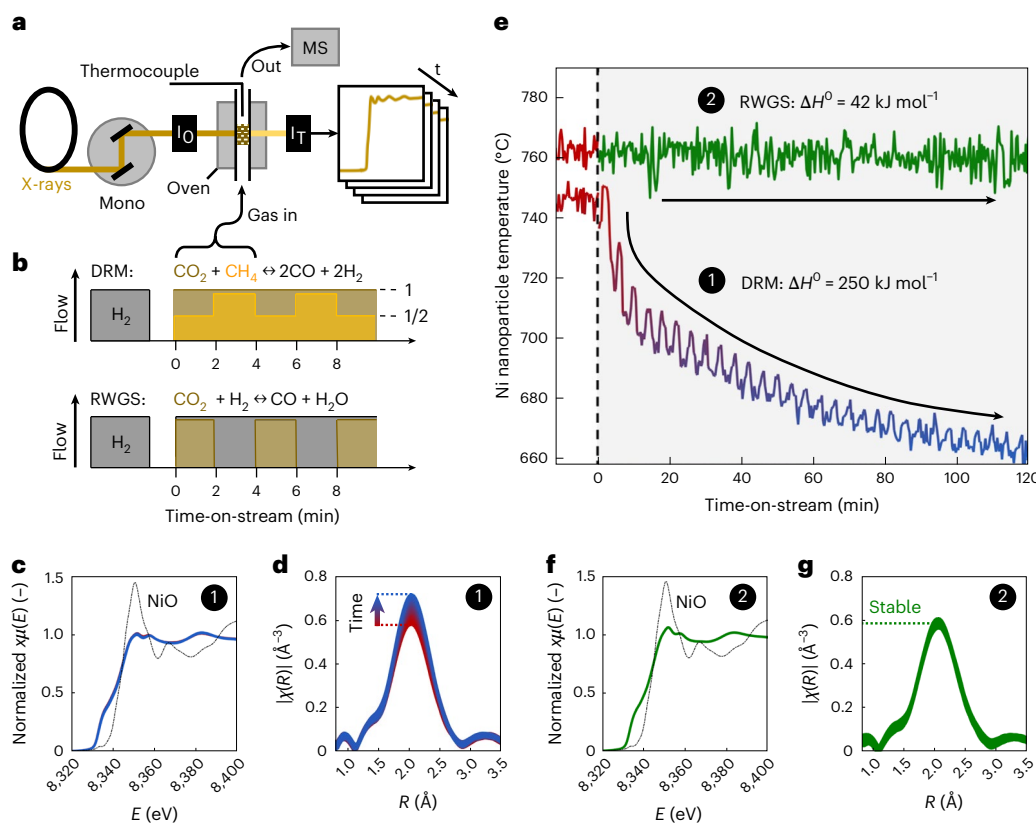


Fig. 3 | Operando EXAFS thermometry to extract the Ni nanoparticle temperature during the DRM and RWGS reactions. **a**, The experimental setup to record synchrotron-based, time-resolved Ni K-edge QXAS. A quartz capillary filled with Ni/MgAl₂O₄ catalyst powder is inserted in an oven with a thermocouple positioned downstream of the catalyst bed. I₀ and I_T represent the incoming and transmitted X-ray intensity, respectively. **b**, Gas flow sequences for the DRM and RWGS reactions at a setpoint temperature of 750 °C, both preceded by a H₂ pre-reduction treatment to reduce the Ni catalyst. For both reactions, gas cycling is applied where the CO₂:CH₄ and CO₂:H₂ ratio are varied. CO₂, CH₄ and

H₂ are labelled in brown, orange and black, respectively. **c,d**, XANES (**c**) and FT EXAFS (**d**) spectral series during the DRM reaction, with the colour scale varying from red to blue over time (0–120 min). **e**, The Ni nanoparticle temperature, extracted via EXAFS thermometry, for both DRM (label 1, red-to-blue coloured line) and RWGS (label 2, green line) reactions. The dashed line indicates the start of the reaction. **f,g**, XANES (**f**) and FT EXAFS (**g**) spectral series during the RWGS reaction, with green colour scale over time. The colour scales in **c, d, f** and **g** are identical to the ones in **e**. The dashed spectrum in **c** and **f** corresponds to a NiO reference.

4 min, and the RWGS (CO₂ + H₂ = CO + H₂O), where the CO₂:H₂ ratio is cycled between 1:1 and 0:1 in a period of 4 min. Both catalysts are operated under low-conversion conditions (<10%) and approach 100% CO selectivity. Before reaction cycling, the Ni catalyst is reduced by H₂ TPR to 800 °C. The gas outlet is connected to a mass spectrometer for product analysis.

For the DRM reaction, the time-resolved X-ray absorption near-edge structure (XANES) and FT EXAFS spectra are plotted in Fig. 3c and Fig. 3d, respectively, with colours evolving from red to blue over time (0–120 min). XANES spectra remain constant and show that the Ni nanoparticles do not undergo phase changes (for example, oxidation), which would make EXAFS thermometry more challenging. The FT EXAFS time series displays a gradual increase in the amplitude of the first Ni coordination shell with time-on-stream, pointing towards a decrease of the Debye–Waller factor and, hence, a decreasing Ni nanoparticle temperature.

Three aspects certify that the FT EXAFS amplitude increase is caused by temperature-induced Debye–Waller factor changes and does not originate from coordination number changes, which could also induce FT EXAFS amplitude changes (Supplementary Note 3): (1) the fitted Ni–Ni coordination number of the FT EXAFS signal before, during and after reaction does not change (Supplementary Fig. 4, Supplementary Tables 1 and 2 and Supplementary Note 4), (2) transmission electron microscopy analysis before and after reaction shows identical Ni nanoparticle size distributions (hence, no size changes; Supplementary

Fig. 3) and (3) no Ni surface oxidation or reduction processes underlie the FT EXAFS amplitude changes (Supplementary Note 5).

Quantitatively mapping the Ni nanoparticle temperature versus the time-on-stream during DRM shows a drastic temperature decrease of the Ni nanoparticles by 90 °C offset to the setpoint temperature of the process over a period of 120 min (Fig. 3e, (1)). In addition, an oscillatory fine structure is superimposed upon the temperature decay, caused by the CO₂:CH₄ ratio cycling (vide infra). Surprisingly, however, the Ni nanoparticle temperature during the RWGS reaction does not show a decrease over time-on-stream, as corroborated by the constant XANES and stable FT EXAFS (Fig. 3f,g,e, (2)).

These findings can be understood by linking these Ni nanoparticle temperature profiles to the DRM and RWGS reaction kinetics. Both DRM ($\Delta H^0 = 250 \text{ kJ mol}^{-1}$) and RWGS ($\Delta H^0 = 42 \text{ kJ mol}^{-1}$) are endothermic processes⁴³, implying that heat is absorbed from the Ni nanoparticles to execute the reaction. The total energy consumption during catalytic reaction equals the reaction enthalpy multiplied by the reaction rate. Hence, a combination of a highly endothermic reaction and a high activity clarifies the strong temperature decrease of Ni nanoparticles during DRM. For the RWGS reaction, the reaction enthalpy is one-fifth of the reaction enthalpy of DRM, but still well beyond 0 kJ mol⁻¹ and, hence, endothermic. A decrease of the Ni nanoparticle temperature would therefore be expected for high RWGS activities, which is not observed. Consequently, a relatively low activity can be held responsible for the stable Ni nanoparticle temperature during the RWGS

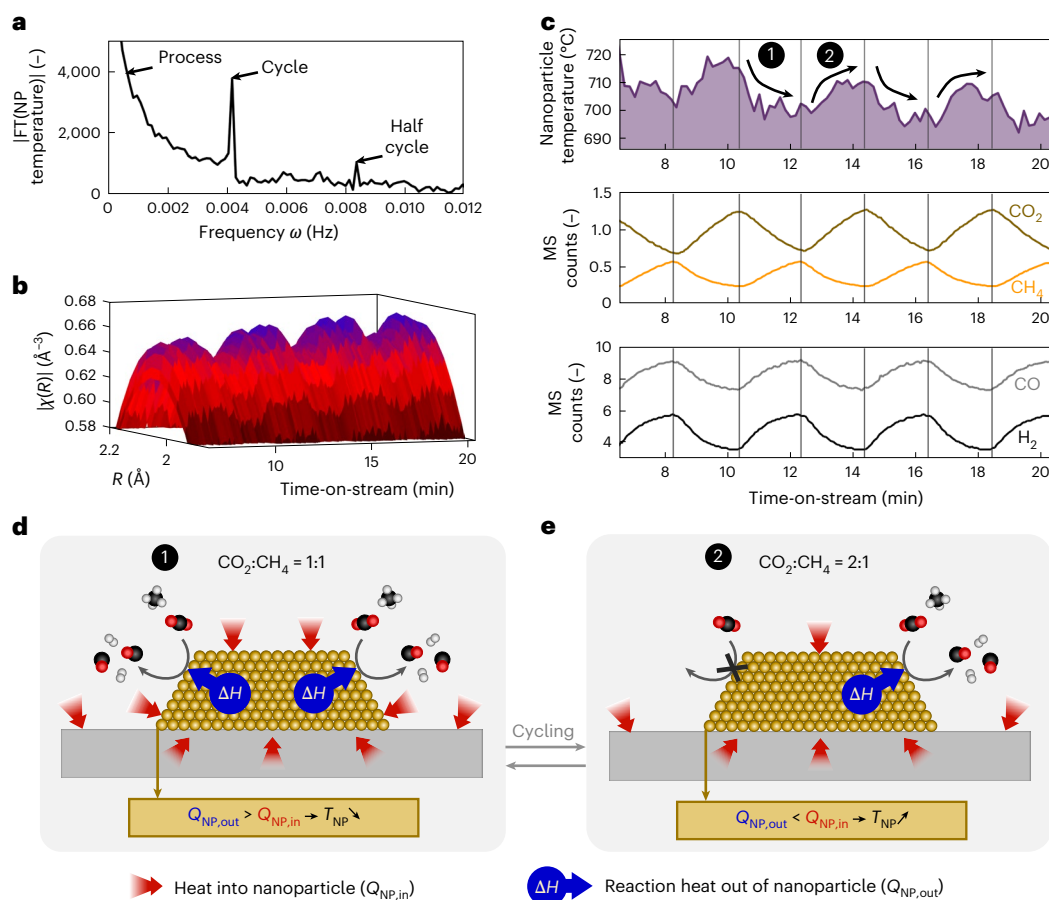


Fig. 4 | Rationalizing the oscillatory temperature and energy balance in Ni nanoparticles during DRM. **a**, The FT signal in the frequency domain of the time-resolved Ni nanoparticle (NP) temperature evolution in Fig. 3c. **b**, Three-dimensional $|\chi(R, t)|$ surface displaying the FT EXAFS magnitude in R space as a function of time-on-stream from -6 to 20 min. **c**, The Ni nanoparticle temperature extracted from **b** as well as the MS signal counts of the input gas feeds of CO_2 and CH_4 and reaction products CO and H_2 . The colour code of

the gases is identical to the one in Fig. 3b. **d, e**, Ni nanoparticle energy states, indicated by the black labels 1 and 2—linking to **c**—for different $\text{CO}_2:\text{CH}_4$ ratios of 1:1 (**d**) and 2:1 (**e**), respectively. The blue symbols indicate reaction heat draining out of the nanoparticle to execute DRM reaction, while the red arrows indicate heat transport into the nanoparticle from the external environment, that is, the gas phase and the support.

reaction, as also suggested by mass spectrometry (Supplementary Fig. 5). Differences in the gas composition between RWGS and DRM reaction could influence the nanoparticle temperature, but do not underlie the discrepancy in the temperature observations between the RWGS and DRM reaction in Fig. 3e (Supplementary Note 6). Therefore, these findings underpin that valuable information can be extracted indirectly on the chemical kinetics of catalysed reactions by monitoring the local temperature of the active phase.

To demonstrate the applicability of EXAFS thermometry at intermediate temperatures, the Ni nanoparticle temperature is monitored during the CO_2 methanation reaction ($\text{CO}_2 + 4\text{H}_2 = \text{CH}_4 + 2\text{H}_2\text{O}$, $\Delta H^\circ = -165 \text{ kJ mol}^{-1}$) at 350°C (Supplementary Note 7, showcase I). The analysis shows a temperature increase of the Ni nanoparticle temperature—as opposed to the DRM and RWGS reactions—resulting from heat release during exothermic reactions. EXAFS thermometry is also applied on Pt_3Sn nanoparticles during RWGS reaction (Supplementary Note 7, showcase II), showing the applicability of the methods on more complex multimetallic catalysis.

Temperature bookkeeping at the nanoparticle level

Extracting the real-time temperature of Ni nanoparticles operando during catalytic reaction now enables one to understand the impact of reaction-induced heat effects on the energy balance of active nanoparticles. The Ni nanoparticle temperature of the DRM process displays

an oscillatory fine structure, which is superimposed on a globally decaying temperature profile (Fig. 3e). To interrogate the periodicity of these oscillations, the Fourier transform of the Ni nanoparticle temperature is depicted in Fig. 4a, showing multiple signal contributions. A broad intensity band is present around 0 Hz, which originates from the globally decaying temperature throughout the entire process (a small ω implies long timescales). In addition, sharp features at -0.004 Hz and -0.008 Hz originate from the periodic Ni temperature oscillations on the timescale of a full cycle ($1/0.004 \text{ s} \approx 240 \text{ s}$ or 4 min) and a half cycle ($1/0.008 \text{ s} \approx 120 \text{ s}$ or 2 min). A full cycle consists of a 2 min half cycle of $\text{CO}_2 + \text{CH}_4$ with $\text{CO}_2:\text{CH}_4$ ratio 2:1, followed by a 2 min half cycle of $\text{CO}_2 + \text{CH}_4$ with $\text{CO}_2:\text{CH}_4$ ratio 1:1. Therefore, the gas cycling frequency clearly correlates with the Ni nanoparticle temperature fluctuations.

The FT EXAFS magnitude versus time-on-stream of the DRM process indeed shows alternating hills and valleys across the $|\chi(R, t)|$ landscape (Fig. 4b). From this $|\chi(R, t)|$ surface, the Ni nanoparticle temperature is extracted (Fig. 4c) and synchronized with the mass spectrometry (MS) counts of the CO_2 and CH_4 reactants and CO and H_2 products. The vertical lines indicate the points in time where the $\text{CO}_2:\text{CH}_4$ ratio is switched from 1:1 to 2:1 and back, displaying a periodically decreasing–increasing–decreasing Ni nanoparticle temperature.

After switching the $\text{CO}_2:\text{CH}_4$ ratio from 2:1 to 1:1 (Fig. 4c, label 1), the CO_2 (CH_4) concentration in the gas flow gradually decreases (increases). Eventually, the gas feed evolves towards an equimolar, stoichiometric

CO₂–CH₄ mixture for the DRM reaction (CO₂ + CH₄ = 2CO + 2H₂), thus maximizing conversion into CO and H₂. Quite the opposite, switching back the CO₂:CH₄ ratio from 1:1 to 2:1 by decreasing the CH₄ flow leads to an excess of CO₂ (Fig. 4c, label 2). This decreases the conversion compared with the CO₂:CH₄ 1:1 case, as evident from the decreasing H₂ and CO MS signals.

Due to gas mixing across the catalyst bed, the CO₂–CH₄ gas feed composition transiently evolves over time, causing non-stationary feed conversion into CO and H₂ (Fig. 4c). Consequently, the Ni nanoparticle temperature also dynamically evolves, because it is conversion dependent. To rationalize the trend in the Ni nanoparticle temperature, the nanoparticle's energy state can be disentangled into two transient regimes (labelled 1 and 2 in Fig. 4d and Fig. 4e, respectively, connecting Fig. 4c). In the regime depicted in Fig. 4d, the CO₂:CH₄ ratio evolves to 1:1, implying a stoichiometric gas feed that maximizes conversion. Given the endothermic nature of the DRM reaction, the reaction heat supplied by the Ni nanoparticle to execute the DRM reaction (blue arrows) exceeds the transfer rate to supply heat to keep the Ni nanoparticle temperature constant (red arrows). This causes a transient decrease in the Ni nanoparticle temperature. In the regime depicted in Fig. 4e, the CO₂:CH₄ ratio evolves to 2:1, implying that CH₄ is present in substoichiometric quantities. Therefore, only half of the DRM reactions can be executed compared with the regime in Fig. 4d, reducing the heat drain from the nanoparticle to the reaction. The heat supply rate from the environment to the nanoparticle now exceeds the consumption rate for reaction, thereby increasing the Ni nanoparticle temperature. By alternating between the CO₂:CH₄ ratios of 1:1 and 2:1, the Ni nanoparticle temperature transiently evolves through both regimes.

The cyclically evolving CO₂–CH₄ gas feed composition can alter the thermal properties of the gas phase, thereby modulating the heat supply from the gas phase to the Ni nanoparticles, which might affect their temperature. In particular, more heat transfer to the Ni nanoparticles is expected under CO₂:CH₄ ratios of 1:1 compared with 2:1, which would lead to a temperature rise under the former conditions (Supplementary Note 6). However, under CO₂:CH₄ ratios of 1:1, the observations in Fig. 4c show that the Ni nanoparticle temperature still declines. Therefore, the more significant reaction-induced cooling under CO₂:CH₄ ratios of 1:1 (due to more DRM reaction than under CO₂:CH₄ = 2:1) still dominates the enhanced gas-induced heating (Fig. 4d, red arrows), leading to a net decrease in the Ni nanoparticle temperature. It is possible, however, that enhanced gas-induced heating could dampen the oscillations in the Ni nanoparticle temperature.

Discussion

The observed temperature changes of active nanoparticles have wide implications. First, active nanoparticles can become a local heat sink or hotspot during endothermic and exothermic reaction. Such temperature deviations in the active phase, offset to the ideal process temperature, can lead to suboptimal^{1,2,4} or degrading^{44,45} performance. Second, temperature deviations can induce structural modifications, such as nanoparticle shape^{46,47} or size^{48,49} changes, hence impacting the number and nature of active sites⁵⁰ at the nanoparticle surface, again impacting performance.

Today, EXAFS thermometry faces two main limitations. First, the technique requires nanoparticles with constant size, because size changes influence the FT EXAFS peak amplitude (Supplementary Note 3). However, multimodal approaches can fully alleviate this limitation by monitoring the nanoparticle size (for example, X-ray scattering) simultaneously with EXAFS thermometry, and correct for nanoparticle size changes. Second, EXAFS thermometry cannot probe the temperature of few-atom clusters or small nanoparticles, where the surface-to-volume ratio approaches 1. In such cases, most atoms of the nanoparticle reside at the surface, which can undergo structural

changes during reaction by reactant or product binding, hence causing EXAFS thermometry to lose accuracy. Therefore, large phase-stable nanoparticles—oxides or metals—are desirable where the surface fraction becomes small.

Despite these challenges, EXAFS thermometry stands out by several advantages compared with state-of-the-art catalysis thermometry methods. First, X-ray absorption spectroscopy (XAS) is element specific, enabling EXAFS thermometry selectively and flexibly at the phase of interest in a broad set of catalytic systems. This enables one to monitor the temperature of the catalytically active phase and the passive support separately to chart temperature discrepancies between different catalyst components. Second, X-rays have higher penetrative power through a material¹⁰ and achieve higher spatial resolution than visible–IR light in luminescence–IR thermometry⁵¹. This endows EXAFS thermometry with the potential to map temperature heterogeneities within catalyst bodies with nanoscale resolution in an element-selective way. Ultimately, temperature bookkeeping can be achieved within complex catalyst bodies by mapping the temperature of individual catalyst components to chart intraparticle heat flows. By extension, temperature heterogeneities on the reactor scale can be mapped under different conditions (dilutions, bed packing strategies and flow rates). Finally, EXAFS thermometry can monitor the temperature of the catalyst as-is, without modification by luminescent sensors. While sophisticated, these sensors might degrade under harsh reaction conditions, are challenging to use when coke is formed or, at worst, participate in reaction. Also, heat transport limitations may arise between the active phase and a spatially remote luminescent sensor, potentially leading to perturbed interpretation.

In summary, this analysis of EXAFS thermometry reveals its capability to selectively monitor the dynamic temperature variations within active Ni nanoparticles during catalytic CO₂ conversion. This method demonstrates significant temperature fluctuations within the nanoparticles responsible for catalysis, indicating that reaction heat directly impacts the energy balance of the nanoparticles, consequently affecting their temperature. In addition, by temperature bookkeeping at the single nanoparticle level, we demonstrate that EXAFS thermometry can extract information on catalytic reaction kinetics. In fact, EXAFS thermometry is an a posteriori analysis approach following time-resolved XAS data collection. Hence, a treasure of temperature information resides in existing XAS datasets worldwide. Revisiting the analysis of these datasets—increasingly available in repositories⁵²—might shine light on reaction-induced temperature phenomena in heterogeneous catalysts and demystify their catalytic consequences.

Methods

Catalyst synthesis

The MgAl₂O₄ support was synthesized through coprecipitation using an aqueous solution of Al(NO₃)₃·9H₂O (ACS reagent, ≥98%, Sigma-Aldrich) and Mg(NO₃)₂·6H₂O (≥99%, Sigma-Aldrich) in accordance with the method described by Theofanidis et al.⁵³. NH₄OH (ACS reagent, 28.0–30.0% NH₃ basis, Sigma-Aldrich) served as precipitating agent to adjust the pH to 10 at 60 °C. After ageing the precipitate for 24 h, it was filtered, dried at 120 °C for 15 h and calcined under flowing air at 800 °C for 5.5 h with a heating rate of 2 °C min⁻¹.

Ni nanoparticles were deposited on MgAl₂O₄ (MgAl₂O₄; sieved 100–150 μm fraction) via wet impregnation using an aqueous solution of Ni(NO₃)₂·6H₂O (99.999%, Sigma-Aldrich) to yield 10 wt% Ni, showing maximal stability in the DRM activity. The catalyst was dried at 120 °C for 3 h and subsequently calcined in air at 800 °C (3 °C min⁻¹) for 1 h. The composition of the catalyst is characterized by inductively coupled plasma analysis and amounts to 9.99 wt% Ni, 13.8 wt% Mg, 30.5 wt% Al and 45.7 wt% O. The resulting Ni/MgAl₂O₄ catalyst is well characterized in previous work⁵⁴, containing additional characterization data such as X-ray diffraction and the Brunauer–Emmett–Teller surface area of the sample termed WI-10Ni/MgAl₂O₄.

QXAS experiments

QXAS measurements were conducted in transmission mode at the ROCK beamline⁵⁵ of the SOLEIL synchrotron (France). The storage ring operated at 2.75 GeV with a ring current of 500 mA in top-up mode. A Frahm monochromator⁵⁶, oscillating at 2 Hz and equipped with a Si(111) monochromator, scanned the Ni K-edge (8,333 eV). This scanning covered both XANES and EXAFS regions in a single scan within the energy range of 8,150–8,970 eV. Calibration was ensured through the measurement of a Ni foil.

In situ and operando QXAS measurements were conducted on the 10 wt% Ni/MgAl₂O₄ catalyst and bulk NiO (≥99.995% trace metals basis, Sigma-Aldrich). To facilitate these measurements, both materials were ground into powders, sieved with a 100–150 μm mesh and diluted to 50% and 95% with boron nitride for 10 wt% Ni/MgAl₂O₄ and NiO, respectively. A 5-mm-long catalyst bed was placed between two quartz wool plugs inside a quartz capillary reactor with a diameter of 1.2 mm (wall thickness 0.010 mm, length 115 mm, Hilgenberg). This capillary reactor was integrated into a dedicated frame, connected to gas feed lines through Swagelok fittings. The entire setup, including the capillary cell, was positioned within a custom-built radiative heating furnace⁴⁰ to achieve the desired reaction temperatures (Fig. 3a). The thermocouple for temperature control of the oven was positioned downstream to the catalyst bed, touching the end of the catalyst bed. The X-ray beam was systematically positioned 2 mm downstream to the start of the catalyst bed, and the catalyst bed was not repositioned with respect to the beam during X-ray experiments. Gas flow rates at the inlet were regulated using calibrated Brooks mass flow controllers, maintaining a total flow rate of 7 ml min⁻¹ for all experiments.

To construct the EXAFS–temperature calibration curves shown in Fig. 2f,i, bulk NiO was first subjected to a H₂ TPR treatment up to 800 °C in 5% H₂/He with a heating rate of 20 °C min⁻¹. This H₂ TPR was followed by a 30 min dwell time at 800 °C to ensure full reduction of NiO into metallic Ni. Subsequently, QXAS spectra were collected during temperature-programmed cooldown (20 °C min⁻¹) of reduced Ni under a constant 5% H₂/He flow, yielding the eventual (FT) EXAFS data and associated EXAFS–temperature calibration curves shown in Fig. 2d–i.

To perform operando EXAFS thermometry, as shown in Figs. 3c–g and 4b,c, the Ni/MgAl₂O₄ catalyst was first reduced during a H₂ TPR in 5% H₂/He up to 800 °C, with a 10 °C min⁻¹ heating rate and dwelled at 800 °C. After reduction treatment, the cell temperature was set to 750 °C in 5% H₂/He to run the catalytic reaction. During DRM (CO₂ + CH₄ = 2CO + 2H₂), 2 min half cycles of 0.7 ml min⁻¹ CH₄ and 1.4 ml min⁻¹ CO₂ in 4.9 ml min⁻¹ He (CO₂:CH₄ = 2:1, total flow rate 7 ml min⁻¹) were alternated with 2 min half cycles of 1.4 ml min⁻¹ CH₄ and 1.4 ml min⁻¹ CO₂ in 4.2 ml min⁻¹ He (CO₂:CH₄ = 1:1, total flow rate 7 ml min⁻¹). A full cycle of DRM thus consisted of 4 min, which was repeated 30 times (Fig. 3e). During RWGS (CO₂ + H₂ = CO + H₂O), 2 min half cycles of 0.5 ml min⁻¹ CO₂ and 2.5 ml min⁻¹ 20% H₂/He in 4 ml min⁻¹ He (CO₂:H₂ = 1:1, total flow rate 7 ml min⁻¹) were alternated with 2 min half cycles of 2.5 ml min⁻¹ 20% H₂/He in 4.5 ml min⁻¹ He (CO₂:CH₄ = 0:1, total flow rate 7 ml min⁻¹). A full cycle of RWGS reaction thus consisted of 4 min, which was repeated 30 times (Fig. 3e).

All QXAS data were recorded with 2 Hz time resolution and averaged over ten spectra to optimize data quality, yielding a 5 s time resolution. All the averaged data were normalized and aligned using the Python normalization graphical user interface, as developed by Roudenko and collaborators⁵⁷.

EXAFS thermometry method

In-house MATLAB scripts were developed to process the normalized XAS spectra to ultimately yield the Ni nanoparticle temperature. Therefore, normalized XAS spectra in energy space were first transformed to *k*²-weighted *k*-space EXAFS signals. These *k*-space EXAFS signals were then Fourier transformed to *R* space by using a Hanning window ($\Delta k = 2 \text{ \AA}^{-1}$ width) from $k = 3 \text{ \AA}^{-1}$ to 11 \AA^{-1} . From the *k*²-weighted FT EXAFS

magnitude, the maximum intensity of the Ni–Ni single scattering peak around 2 Å (non-phase corrected) was evaluated as a function of time-on-stream. By using a calibration curve between the natural logarithm of this Ni–Ni maximum and the Ni temperature, the temperature could be extracted. In Fig. 3e, it is observed that a 15 °C difference in the Ni nanoparticle temperature is observed before the DRM (–745 °C) and RWGS (–760 °C) reaction, which is explained in Supplementary Note 8.

Transmission electron microscopy

Scanning transmission electron microscopy was used to examine the Ni nanoparticle size of the Ni/MgAl₂O₄ catalyst (Supplementary Fig. 3). The imaging was recorded using a Cs-corrected JEOL JEM-2200FS equipped with a Schottky-type field-emission gun and a JEOL JED-2300D Energy Dispersive X-ray Analysis detector, operating at 200 kV. The catalyst under investigation was deposited on a lacey carbon film mounted on a copper grid by immersing the grid into the catalyst powder.

Mass spectrometry

The gas outlet composition was measured using an online quadrupole mass spectrometer (Cirrus, MKS). CO₂, CO, H₂O, CH₄, He and H₂ were calculated from the *m/z* signal collected for 44, 28, 18, 16, 4 and 2, respectively.

Data availability

All data are available from the corresponding authors upon reasonable request.

Code availability

Code to perform EXAFS thermometry is available via GitHub at <https://github.com/matthiasfilez/EXAFS-thermometry>.

References

1. Dumesic, J. A., Huber, G. W. & Boudart, M. *Handbook of Heterogeneous Catalysis* (Wiley, 2008).
2. Somorjai, G. A. & Li, Y. *Introduction to Surface Chemistry and Catalysis* (Wiley, 2010).
3. Nørskov, J. K. et al. The nature of the active site in heterogeneous metal catalysis. *Chem. Soc. Rev.* **37**, 2163–2171 (2008).
4. Marin, G. B. & Yablonsky, G. *Kinetics of Chemical Reactions: Decoding Complexity* (Wiley, 2011).
5. Liu, L. & Corma, A. Metal catalysts for heterogeneous catalysis: from single atoms to nanoclusters and nanoparticles. *Chem. Rev.* **118**, 4981–5079 (2018).
6. Bañares, M. A. Operando spectroscopy: the knowledge bridge to assessing structure–performance relationships in catalyst nanoparticles. *Adv. Mater.* **23**, 5293–5301 (2011).
7. Groppo, E., Rojas-Buzo, S. & Bordiga, S. The role of in situ/operando IR spectroscopy in unraveling adsorbate-induced structural changes in heterogeneous catalysis. *Chem. Rev.* **123**, 12135–12169 (2023).
8. Buurmans, I. L. C. & Weckhuysen, B. M. Heterogeneities of individual catalyst particles in space and time as monitored by spectroscopy. *Nat. Chem.* **4**, 873–886 (2012).
9. Singh, J., Lamberti, C. & van Bokhoven, J. A. Advanced X-ray absorption and emission spectroscopy: in situ catalytic studies. *Chem. Soc. Rev.* **39**, 4754–4766 (2010).
10. Meirer, F. & Weckhuysen, B. M. Spatial and temporal exploration of heterogeneous catalysts with synchrotron radiation. *Nat. Rev. Mater.* **3**, 324–340 (2018).
11. Werghi, B. et al. Selective catalytic behavior induced by crystal-phase transformation in well-defined bimetallic Pt–Sn nanocrystals. *Small* **19**, 2207956 (2023).
12. Filez, M. et al. Formation and functioning of bimetallic nanocatalysts: the power of X-ray probes. *Angew. Chem. Int. Ed.* **58**, 13220–13230 (2019).

13. Roldan Cuenya, B. Metal nanoparticle catalysts beginning to shape-up. *Acc. Chem. Res.* **46**, 1682–1691 (2013).
14. Sarma, B. B., Maurer, F., Doronkin, D. E. & Grunwaldt, J.-D. Design of single-atom catalysts and tracking their fate using operando and advanced X-ray spectroscopic tools. *Chem. Rev.* **123**, 379–444 (2023).
15. Timoshenko, J. & Roldan Cuenya, B. In situ/operando electro-catalyst characterization by X-ray absorption spectroscopy. *Chem. Rev.* **121**, 882–961 (2021).
16. Urakawa, A. & Baiker, A. Space-resolved profiling relevant in heterogeneous catalysis. *Top. Catal.* **52**, 1312–1322 (2009).
17. Mitchell, S., Qin, R., Zheng, N. & Pérez-Ramírez, J. Nanoscale engineering of catalytic materials for sustainable technologies. *Nat. Nanotechnol.* **16**, 129–139 (2021).
18. Marberger, A. et al. Time-resolved copper speciation during selective catalytic reduction of NO on Cu-SSZ-13. *Nat. Catal.* **1**, 221–227 (2018).
19. Potter, M. E. et al. A high pressure operando spectroscopy examination of bimetal interactions in ‘metal efficient’ palladium/ $\text{In}_2\text{O}_3/\text{Al}_2\text{O}_3$ catalysts for CO_2 hydrogenation. *Angew. Chem. Int. Ed.* **62**, e202312645 (2023).
20. Qi, G. et al. Au-ZSM-5 catalyses the selective oxidation of CH_4 to CH_3OH and CH_3COOH using O_2 . *Nat. Catal.* **5**, 45–54 (2022).
21. Wei, J. On the maximum temperature inside a porous catalyst. *Chem. Eng. Sci.* **21**, 1171–1183 (1966).
22. Grunwaldt, J.-D., Wagner, J. B. & Dunin-Borkowski, R. E. Imaging catalysis at work: a hierarchical approach from the macro- to the meso- and nano-scale. *ChemCatChem* **5**, 62–80 (2013).
23. Tiburski, C., Nugroho, F. A. A. & Langhammer, C. Optical hydrogen nanothermometry of plasmonic nanoparticles under illumination. *ACS Nano* **16**, 6233–6243 (2022).
24. Georgiades, G., Self, V. A. & Sermon, P. A. IR emission analysis of temperature profiles in Pt/ SiO_2 catalysts during exothermic reactions. *Angew. Chem. Int. Ed.* **26**, 1042–1043 (1987).
25. Simeone, M., Salemme, L. & Allouis, C. Reactor temperature profile during autothermal methane reforming on Rh/ Al_2O_3 catalyst by IR imaging. *Int. J. Hydrogen Energy* **33**, 4798–4808 (2008).
26. Hannemann, S. et al. Axial changes of catalyst structure and temperature in a fixed-bed microreactor during noble metal catalysed partial oxidation of methane. *Top. Catal.* **52**, 1360–1370 (2009).
27. Geitenbeek, R. G. et al. In situ luminescence thermometry to locally measure temperature gradients during catalytic reactions. *ACS Catal.* **8**, 2397–2401 (2018).
28. Hartman, T., Geitenbeek, R. G., Whiting, G. T. & Weckhuysen, B. M. Operando monitoring of temperature and active species at the single catalyst particle level. *Nat. Catal.* **2**, 986–996 (2019).
29. Hartman, T., Geitenbeek, R. G., Wondergem, C. S., van der Stam, W. & Weckhuysen, B. M. Operando nanoscale sensors in catalysis: all eyes on catalyst particles. *ACS Nano* **14**, 3725–3735 (2020).
30. Terlingen, B. J. P. et al. Bifunctional europium for operando catalyst thermometry in an exothermic chemical reaction. *Angew. Chem. Int. Ed.* **61**, e202211991 (2022).
31. Jacobs, T. S. et al. Mapping temperature heterogeneities during catalytic CO_2 methanation with operando luminescence thermometry. *ACS Nano* **17**, 20053–20061 (2023).
32. Munnik, P., de Jongh, P. E. & de Jong, K. P. Recent developments in the synthesis of supported catalysts. *Chem. Rev.* **115**, 6687–6718 (2015).
33. Koptjug, I. V., Khomichev, A. V., Lysova, A. A. & Sagdeev, R. Z. Spatially resolved NMR thermometry of an operating fixed-bed catalytic reactor. *J. Am. Chem. Soc.* **130**, 10452–10453 (2008).
34. Cale, T. S. Nickel crystallite thermometry during ethane hydrogenolysis. *J. Catal.* **90**, 40–48 (1984).
35. Van de Broek, B. et al. Temperature determination of resonantly excited plasmonic branched gold nanoparticles by X-ray absorption spectroscopy. *Small* **7**, 2498–2506 (2011).
36. Rosen, D. J., Yang, S., Marino, E., Jiang, Z. & Murray, C. B. In situ EXAFS-based nanothermometry of heterodimer nanocrystals under induction heating. *J. Phys. Chem. C* **126**, 3623–3634 (2022).
37. Espinosa, A. et al. Photoactivated nanoscale temperature gradient detection using X-ray absorption spectroscopy as a direct nanothermometry method. *Nano Lett.* **21**, 769–777 (2021).
38. Ano, T. et al. Probing the temperature of supported platinum nanoparticles under microwave irradiation by in situ and operando XAFS. *Commun. Chem.* **3**, 86 (2020).
39. López-Méndez, R. et al. X-ray nanothermometry of nanoparticles in tumor-mimicking tissues under photothermia. *Adv. Healthc. Mater.* **12**, 2301863 (2023).
40. La Fontaine, C., Belin, S., Barthe, L., Roudenko, O. & Briois, V. ROCK: a beamline tailored for catalysis and energy-related materials from ms time resolution to μm spatial resolution. *Synchrotron Radiat. News* **33**, 20–25 (2020).
41. Koningsberger, D. C., Mojet, B. L., Van Dorssen, G. E. & Ramaker, D. E. XAFS spectroscopy; fundamental principles and data analysis. *Top. Catal.* **10**, 143–155 (2000).
42. Rehr, J. J. Theoretical approaches to X-ray absorption fine structure. *Rev. Mod. Phys.* **72**, 621–654 (2000).
43. Pinto, D., Hu, L. & Urakawa, A. Enabling complete conversion of CH_4 and CO_2 in dynamic coke-mediated dry reforming (DC-DRM) on Ni catalysts. *Chem. Eng. J.* **474**, 145641 (2023).
44. Martín, A. J., Mitchell, S., Mondelli, C., Jaydev, S. & Pérez-Ramírez, J. Unifying views on catalyst deactivation. *Nat. Catal.* **5**, 854–866 (2022).
45. Filez, M. et al. Nanoscale chemical diversity of coke deposits on nanoprinted metal catalysts visualized by tip-enhanced Raman spectroscopy. *Adv. Mater.* **36**, 2305984 (2024).
46. Duan, M. et al. Reconstruction of supported metal nanoparticles in reaction conditions. *Angew. Chem. Int. Ed.* **57**, 6464–6469 (2018).
47. Chmielewski, A. et al. Reshaping dynamics of gold nanoparticles under H_2 and O_2 at atmospheric pressure. *ACS Nano* **13**, 2024–2033 (2019).
48. Solano, E. et al. Metal nanocatalyst sintering interrogated at complementary length scales. *Small* **19**, 2205217 (2023).
49. Dai, Y., Lu, P., Cao, Z., Campbell, C. T. & Xia, Y. The physical chemistry and materials science behind sinter-resistant catalysts. *Chem. Soc. Rev.* **47**, 4314–4331 (2018).
50. Vogt, C. & Weckhuysen, B. M. The concept of active site in heterogeneous catalysis. *Nat. Rev. Chem.* **6**, 89–111 (2022).
51. Tian, Y. et al. Spatiotemporal heterogeneity of temperature and catalytic activation within individual catalyst particles. *J. Am. Chem. Soc.* **146**, 4958–4972 (2024).
52. Taniike, T. & Takahashi, K. The value of negative results in data-driven catalysis research. *Nat. Catal.* **6**, 108–111 (2023).
53. Theofanidis, S. A., Galvita, V. V., Poelman, H. & Marin, G. B. Enhanced carbon-resistant dry reforming Fe–Ni catalyst: role of Fe. *ACS Catal.* **5**, 3028–3039 (2015).
54. De Coster, V., Srinath, N. V., Yazdani, P., Poelman, H. & Galvita, V. V. Does CO_2 oxidize Ni catalysts? A quick X-ray absorption spectroscopy answer. *J. Phys. Chem. Lett.* **13**, 7947–7952 (2022).
55. Briois, V. et al. ROCK: the new Quick-EXAFS beamline at SOLEIL. *J. Phys. Conf. Ser.* **712**, 012149 (2016).
56. Stötzl, J., Lützenkirchen-Hecht, D. & Frahm, R. A new flexible monochromator setup for quick scanning X-ray absorption spectroscopy. *Rev. Sci. Instrum.* **81**, 073109 (2010).
57. Lesage, C. et al. High pressure cell for edge jumping X-ray absorption spectroscopy: applications to industrial liquid sulfidation of hydrotreatment catalysts. *Catal. Today* **336**, 63–73 (2019).

Acknowledgements

M.F. acknowledges the FWO for a senior postdoctoral research fellowship (1280621N). This work was supported by the Fund for Scientific Research Flanders (grant no. GOA5923N (M.B.J.R. and C.D.), 3G021220 (V.G. and C.D.), G093823N (M.F. and J.D.)) and the Special Research Fund BOF of Ghent University (grant no. GOA-01G02124 (M.F., J.D. and C.D.)). The research leading to these results is supported by the project CALIPSOplus under grant agreement 730872 from the EU Framework Programme for Research and Innovation HORIZON 2020, in supplying financing of subsistence costs for the synchrotron campaign (SOLEIL, proposal 20200555 (V.D.C., H.P. and V.G.)). We acknowledge the assistance from the ROCK staff for a smooth beamtime.

Author contributions

M.F., J.D., M.B.J.R. and C.D. conceived the research idea and project. V.D.C., H.P. and V.G. produced the samples and collected the XAS data together with V.B. and A.B. M.F., V.D.C. and A.B. preprocessed the data. M.F. developed the thermometry workflow and data analysis with the support of V.D.C. M.F. and V.G. collected the transmission electron microscopy data. M.F. analysed the transmission electron microscopy data and wrote the paper. All authors contributed to revising and optimizing the paper.

Competing interests

The authors declare no competing interests.

Additional information

Supplementary information The online version contains supplementary material available at <https://doi.org/10.1038/s41929-025-01295-9>.

Correspondence and requests for materials should be addressed to Matthias Filez or Christophe Detavernier.

Peer review information *Nature Catalysis* thanks Ken Motokura and the other, anonymous, reviewer(s) for their contribution to the peer review of this work.

Reprints and permissions information is available at www.nature.com/reprints.

Publisher's note Springer Nature remains neutral with regard to jurisdictional claims in published maps and institutional affiliations.

Springer Nature or its licensor (e.g. a society or other partner) holds exclusive rights to this article under a publishing agreement with the author(s) or other rightsholder(s); author self-archiving of the accepted manuscript version of this article is solely governed by the terms of such publishing agreement and applicable law.

© The Author(s), under exclusive licence to Springer Nature Limited 2025